



- 1 Strong monsoon influence on South Asian methane emissions
- 2 in 2020 revealed by a Bayesian inversion constrained by
- **satellite observations**
- 4 Rakesh Subramanian<sup>1</sup>, Rona L. Thompson<sup>2</sup>, Martin Vojta<sup>1</sup>, Oliver Schneising<sup>3</sup> and Andreas
- 5 Stohl<sup>1</sup>
- 6 Department of Meteorology and Geophysics, University of Vienna, Vienna, Austria.
- 7 Norwegian Institute for Air Research (NILU), Kjeller, Norway.
- 8 <sup>3</sup> University of Bremen, Bremen, Germany.
- 9 Correspondence to: Rakesh Subramanian (rakesh.subramanian@univie.ac.at)

### Abstract

- 12 South Asia is a major contributor to global methane (CH4) emissions, yet its emissions remain poorly constrained,
- 13 limiting targeted mitigation. Current bottom-up inventories do not consistently capture the magnitude and
- 14 seasonality of CH<sub>4</sub> emissions in this region, particularly during the monsoon. Here we quantify South Asian CH<sub>4</sub>
- emissions for 2020 using column observations from TROPOMI, a Lagrangian transport model (FLEXPART),
- and a Bayesian inversion system (FLEXINVERT+). We estimate a posteriori emission of  $73.0 \pm 0.5 \text{ Tg yr}^{-1}$  for
- 17 South Asia, including 35.6 ± 0.5 Tg yr<sup>-1</sup> for India and 13.2 ± 0.2 Tg yr<sup>-1</sup> for Bangladesh. Agriculture and wetlands
- 18 contribute substantially to the regional budget, with the flux increments coincident with rice-growing areas and
- 19 inundated lowlands. The inversion indicates pronounced monsoon-modulated seasonality: posterior fluxes are
- 20 higher than the prior during June-September by ~70% and lower during January-May by ~46%. Localized
- 21 enhancements seen over the lower Indus Basin align with runoff patterns, while the seasonal peaks here are absent
- 22 in inventories. By resolving monsoon seasonality with satellite constraints, our results point towards key
- 23 uncertainties in the South Asian CH4 budget and underscore the need for process-based, seasonally responsive
- 24 inventories to inform mitigation strategies and reconcile bottom-up and top-down estimates.

### 1. Introduction

25

- Methane (CH<sub>4</sub>) is a potent greenhouse gas with a global warming potential 85 times higher than that of carbon
- 27 dioxide over a 20-year period. Understanding and accurately quantifying methane emissions is therefore crucial
- 28 for developing effective climate mitigation strategies. South Asia (SA), with its diverse sources of methane
- emissions, including agriculture, waste, wetlands, energy production and use, presents a unique and complex
- domain for such studies. This region includes India, Pakistan, Bangladesh, Nepal, Bhutan and Sri Lanka. SA is
- 31 one of the biggest methane emission hotspots in the world [Stavert et al., 2020], with its total emissions rising
- 32 from 37 Tg yr $^{-1}$  in the 2000s to 75 Tg yr $^{-1}$  in the 2010s [Belikov et al., 2024]. Patra et al. (2013) estimated  $37\pm3.7$
- Tg yr $^{-1}$  during the 2000s and Wang et al. (2021) estimated  $64.35 \pm 9.28$  Tg yr $^{-1}$  emissions from the year 2009 to
- 2018 over South Asia. Among Asian countries, this region contributes to about 25.6% of the total budget for 2001-2021 [Ito et al., 2023]. As all of these are developing nations, their economic growth causes a notable rise
- in anthropogenic emissions, particularly from agriculture.





India, the largest economy of the region, contributes more than half of these emissions, and is the key region of focus in this study. This region has been the focus of several country-scale studies (Fig. 1). Ganesan et al. (2017) estimated average methane emissions of 22.0 (19.6–24.3) Tg yr<sup>-1</sup> during 2010–2015, while Raju et al. (2022) reported ~10.63 Tg yr<sup>-1</sup> of methane emissions from Peninsular India (south of 21.5°N) for 2017–2018. More recent satellite-based studies give higher values, with Worden et al. (2022) estimating 39.5 ± (2.8–5.4) Tg yr<sup>-1</sup> of anthropogenic emissions for the year 2019 and Yu et al. (2023) reporting 36 (34–38) Tg yr<sup>-1</sup> of anthropogenic emissions for 2018–2019. India's National Communication reports its anthropogenic greenhouse gas emissions to UNFCCC in the form of Biennial Update Reports (BUR). These bottom-up reports estimate emissions of 19.8, 20.05, 19.55 and 18.8 Tg yr<sup>-1</sup>, respectively, for the years 2010, 2014, 2016 and 2020. The country's report also includes the top-down anthropogenic methane estimate of 24.2±5.3 Tg yr<sup>-1</sup> for the years 2011-2017, taken from Janardanan et al. (2020). Figure 1 shows the estimation of methane emissions for India from various literature reports. While there are not many studies over other regions of South Asia, Peters et al. (2017) report emissions for Bangladesh in the range of 1.3 to 3.1 Tg yr<sup>-1</sup> for the 2000s.

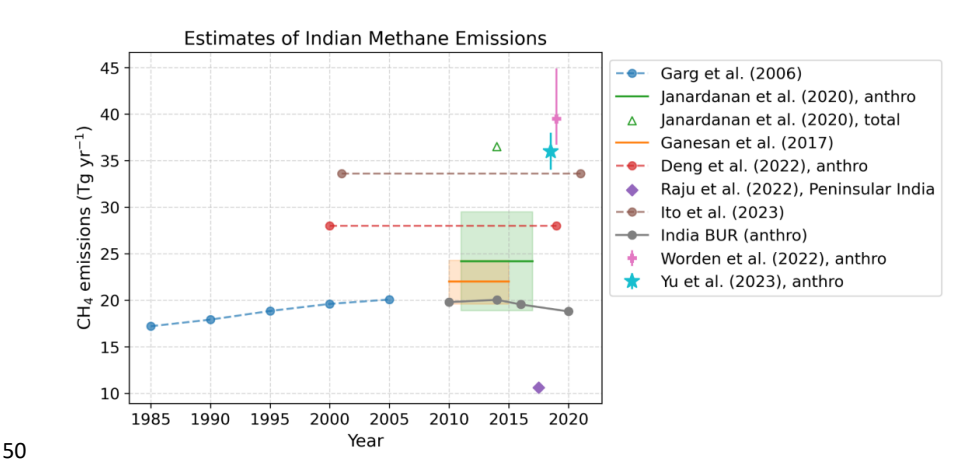


Figure 1. Literature estimates of Indian methane (CH<sub>4</sub>) emissions. Shaded regions and bars indicate uncertainties, where available. The estimates underscore significant heterogeneity across methodologies and observation periods.

In a situation where bottom-up emission inventories are highly uncertain, top-down methods based on atmospheric measurements offer the possibility to verify or improve the bottom-up inventories. However, while regions like Europe and North America are covered with relatively dense ground-based GHG monitoring networks, only a few stations exist in South Asia. Moreover, access to high-quality data from the few existing sites is often limited or difficult, further hindering reliable budget estimates.

The earliest satellite observations for methane were provided by the SCanning Imaging Absorption spectroMeter for Atmospheric CHartographY (SCIAMACHY) instrument onboard the ENVISAT satellite, launched in 2002. The launch of the first dedicated greenhouse gas monitoring satellite, GOSAT (Greenhouse Gases Observing Satellite), in 2009 opened the possibility for monitoring carbon dioxide and methane emissions across the globe. Since then, several other satellites have enhanced the GHG monitoring capabilities. The TROPOspheric Monitoring Instrument (TROPOMI) on the Sentinel-5 Precursor satellite, launched in October 2017, provides





- 64 high-resolution, daily global observations of atmospheric methane. The TROPOMI data offer unprecedented
- 65 spatial and temporal coverage well suited for GHG estimation both on global and regional scales.
- This study is one of the first to leverage TROPOMI satellite observations with a Lagrangian transport model to
- 67 constrain the methane budget over South Asia. The study is conducted for the year 2020 and employs the transport
- 68 model FLEXPART and the Bayesian inversion framework Flexinvert+ to estimate the methane fluxes. With this
- 69 setup, we seek to enhance our understanding of regional methane dynamics, address the discrepancies between
- 70 the bottom-up emission estimates and the observed atmospheric mole fractions and thereby contribute to the
- 71 development of more effective climate policies.

### 72 2. Data and Methods

73

### 2.1 Methane Observations

- 74 The TROPOMI instrument onboard the Sentinel-5P satellite is in a sun-synchronous orbit which uses the short-
- wavelength infrared spectral region (2305-2385 nm) to detect CH<sub>4</sub>. It has a swath width of 2600 km and a spatial
- 76 resolution of 7 x 5.5 km². The column-averaged dry-air mole fraction of methane, XCH4, represents a measure of
- 77 the average methane mole fraction across the atmospheric column. This study uses the TROPOMI data based on
- 78 the WFM-DOAS retrieval algorithm (TROPOMI/WFMD) version 1.8 [Schneising et al., 2023]. This least-
- 79 squares method fits a linearised radiative transfer model, together with a low-degree polynomial, to the logarithm
- 80 of the measured sun-normalised radiance through the scaling of previously selected atmospheric vertical profiles.
- 81 Fast retrievals are facilitated by a look-up table of tabulated reference spectra and their derivatives (weighting
- 82 functions) with respect to the fit parameters for a variety of typical atmospheric conditions. Since the look-up
- 83 table is limited to certain atmospheric conditions such as cloud-free scenes, a binary machine learning-based
- quality filter was implemented, which was trained in a one-time process using quasi-simultaneous cloud information from the Visible Infrared Imaging Radiometer Suite (VIIRS) on board Suomi NPP and can
- 86 subsequently be applied independently of VIIRS data [Schneising et al., 2019]. TROPOMI/WFMD has
- 87 historically offered better coverage in certain regions and seems to be less affected by specific biases (e.g.,
- 88 concerning spectral albedo variability, striping artefacts, seasonal effects) compared with the operational data
- product [Schneising et al., 2023; Lindqvist et al. 2024].
- 90 The data over the study domain (5° to 38°N and 60° to 98°E) comprises approximately 10,000 to 80,000 soundings
- 91 per day for the year 2020, with a maximum number in November and December and a minimum from June to
- 92 September (JJAS). The poorer data coverage in the JJAS period is due to the presence of monsoonal clouds. Figure
- 93 2 shows the spatial distribution of valid TROPOMI observations across the study domain for the four seasons
- 94 winter (JF), pre-monsoon (MAM), monsoon (JJAS) and post-monsoon (OND). The retrieved XCH4 mole
- 95 fractions are highest from June to December, and the largest values are detected over northern and eastern parts
- 96 of India, Pakistan and Bangladesh.





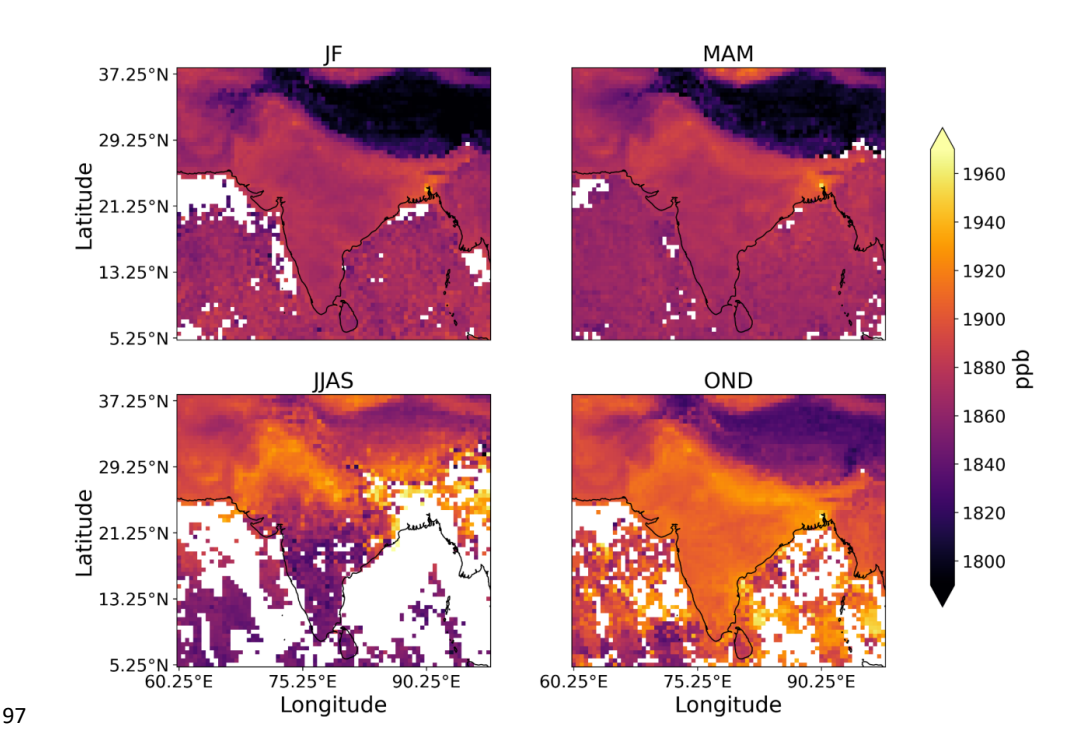


Figure 2. Seasonal mean TROPOMI methane column-averaged dry air mole fractions (XCH<sub>4</sub>), averaged over  $0.5^{\circ}$  x  $0.5^{\circ}$  grid cells over South Asia. White areas indicate grid cells without observations due to cloud cover and missing retrievals over the ocean.

## 2.1.1 Selection of Observation

We only used satellite retrievals flagged as good quality (quality flag = 0). In addition, the column observations over the Himalayan mountains are also excluded because the highly variable topography makes the retrievals more uncertain. Figure 3(a) shows a time series of monthly mean TROPOMI observed XCH<sub>4</sub> over the study domain. The second half of the year has higher methane mole fractions, likely reflecting increased methane emissions due to the agricultural practices and inundation of wetlands after the monsoon rainfall. The total number of retrievals for the whole domain after filtering amounts to approximately 9 million. This vast amount of data would add a prohibitive computational load for the models used in the study, while often delivering redundant information. In order to reduce the number of observations while preserving most of the information content, the retrievals are aggregated and averaged spatially on a 0.25° x 0.25° and a 0.50° x 0.50° latitude/longitude variable grid based on the spatial variability of methane mole fractions. Essentially, the mean and standard deviation of the column mole fractions are calculated at the coarsest grid box (0.5°). When the standard deviation in the coarsest grid exceeds a certain threshold (15ppb), the grid is further divided into a finer grid. This two-resolution step approach is done to ensure that the grid cells with a higher variability of methane mole fractions are separately taken into account. An example of such a variable grid is shown in Fig. 3(b). This method is explained in detail in Thompson et al. (2025), and the aggregated observations from now are called super-observations.



119

120

121

122

123

124

125

126

127

128 129

130

131

132

133134

135

136137

138139

140

141

142143



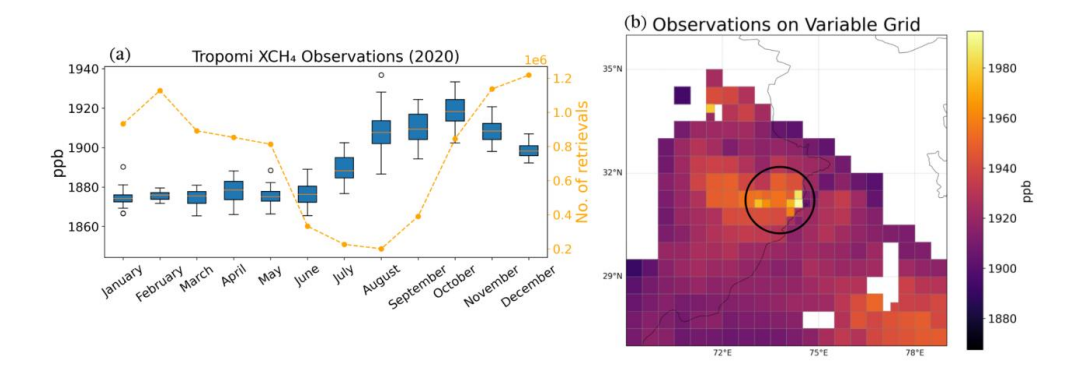


Figure 3. a) Seasonality of the observed TROPOMI methane column mole fractions (XCH<sub>4</sub>) averaged over the whole domain. The blue boxes represent the interquartile range (IQR), the center line the median, the whiskers represent the most extreme data points within  $1.5 \times IQR$  of the monthly mole fractions and the circles are outliers. Also shown is the number of retrievals in each month (orange line). b) Observations aggregated on a variable resolution latitude/longitude grid  $(0.25^{\circ} \times 0.25^{\circ})$  and  $0.50^{\circ} \times 0.50^{\circ})$  for a typical day in October. The black circle shows a region where the fine grid is used with larger heterogeneity in mole fractions.

# 2.2 Methane Prior Fluxes

To supply the inversion system with prior methane fluxes, we used bottom-up inventories for eight different source categories: (1) anthropogenic emissions from Edgar version 8 [Crippa et al., 2023], (2) wetland emissions from the NASA Earth Observation SIMulator version of the Lund-Potsdam-Jena Dynamic Global Vegetation Model - LPJ EOSIM [Colligan et al., 2024], (3) fire emissions from Finn [Wiedinmyer et al., 2023], (4) geological emissions [Etiope et al., 2019], (5) termite emissions from CAMS [Granier et al., 2019], (6) emissions from rivers and streams [Rocher-Ros et al., 2023], (7) shallow coastal water ocean emissions [Weber et al., 2019], and (8) soil sink from the Soil Methanotrophy Model - MeMo v1 [Murguia-Flores et al., 2018]. Annual mean maps of all these fluxes are shown in Fig. 4 and total numbers are reported in Table 1. The sums of the fluxes from all source categories were provided to the model at a spatial resolution of 0.5° x 0.5° and at monthly time steps. The net global total methane flux from all these sectors together is 612.5 Tg yr<sup>-1</sup>, of which 66.3 Tg yr<sup>-1</sup> are emitted in the study region (5° to 38°N and 60° to 98°E). A breakdown of the methane flux sources reveals that anthropogenic sources dominate the emissions over the study domain, contributing 50.64 Tg yr<sup>-1</sup>, which accounts for over 76% of the total regional methane budget of 66.3 Tg yr<sup>-1</sup>. The sub-sectors of anthropogenic emissions include mainly agriculture emissions (33.7 Tg yr<sup>-1</sup>) and waste emissions (10.3 Tg yr<sup>-1</sup>) followed by fuel production and usage in industries, transport and buildings (Sup. Fig. 1). Wetlands contribute 13.2 Tg yr<sup>-1</sup>, making them the largest natural source of methane in the region. Other sources such as fires (1.6 Tg yr<sup>-1</sup>), geological sources (0.8 Tg yr<sup>-1</sup>), and termites (0.9 Tg yr<sup>-1</sup>) contribute smaller but non-negligible portions to the total emissions. Emissions from rivers (0.6 Tg yr<sup>-1</sup>) and oceans (0.3 Tg yr<sup>-1</sup>) are relatively minor, while the soil sink (-1.7 Tg yr<sup>-1</sup>) represents a modest removal flux.



148



The spatial distribution of these fluxes shows anthropogenic emissions are dominant over the river plains of northeastern India, Bangladesh and Pakistan. Bangladesh also has high wetland emissions. Notably high landfill emissions can also be found over the capital city of India, Delhi.

Methane Flux	Dataset / Reference	Global Total (Tg yr <sup>-</sup> 1)	Study Domain Total (Tg yr <sup>-1</sup> )
Anthropogenic	Edgar v8 – [Crippa et al., 2023]	352.70	50.64
Wetlands	NASA LPJ-EOSIM – [Colligan et al., 2024]	187.10	13.19
Fire	FINN – [Wiedinmyer et al., 2023]	25.98	1.58
Geological	Etiope et al., 2019	36.04	0.82
Termites	CAMS – [Granier et al., 2019]	19.65	0.92
Rivers	[Rocher-Ros et al., 2023]	10.99	0.61
Ocean	Weber et al., 2019	9.23	0.27
Soil Sink	MeMo v1.0 – [Murguia-Flores et al., 2018]	-29.24	-1.69
Total	_	612.45	66.34

Table 1. Total methane fluxes for the eight sectors used to construct our a priori emissions for the year 2020 globally and for our study domain (5° to  $38^\circ N$ ,  $60^\circ$  to  $98^\circ E$ ).



151



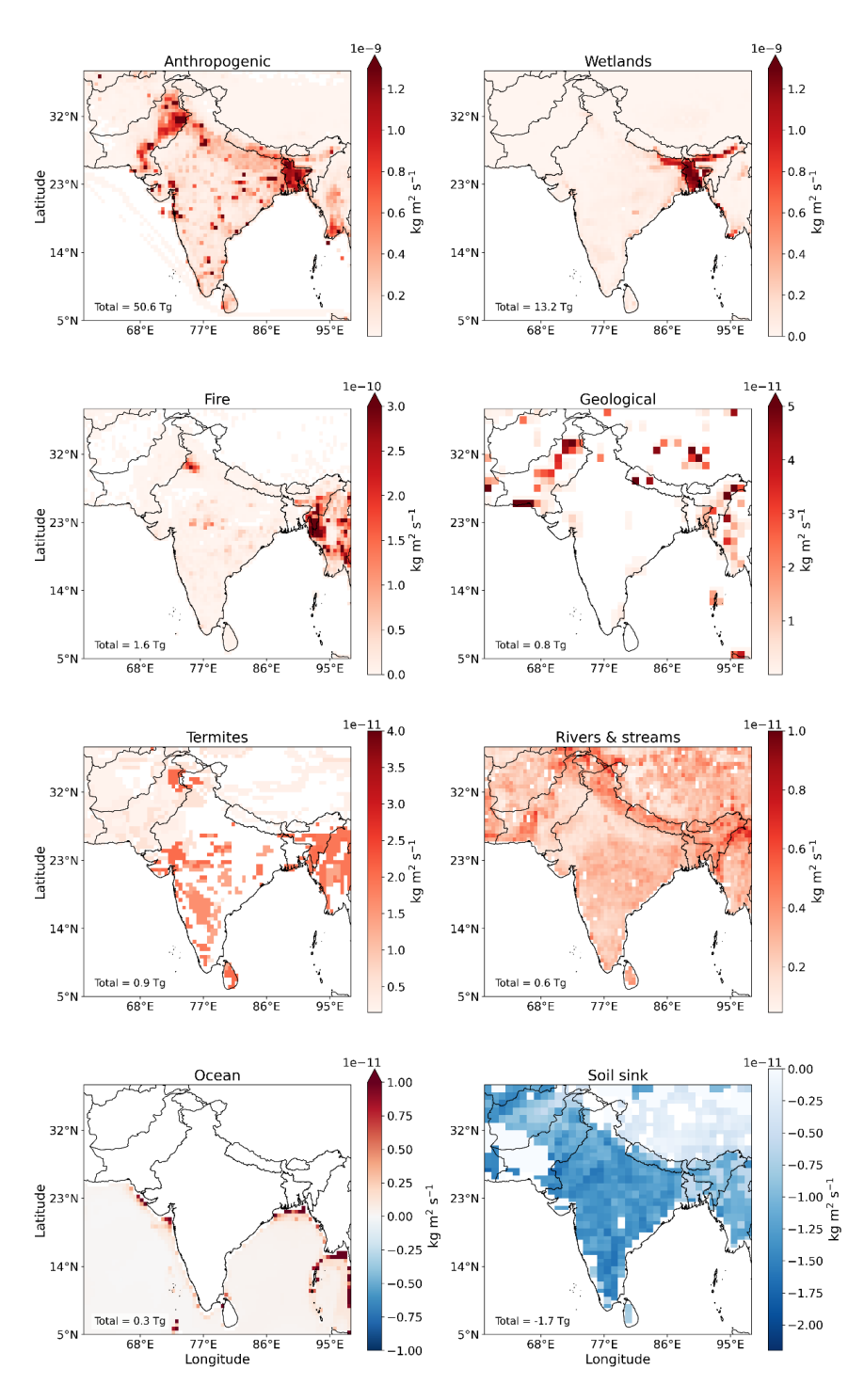


Figure 4. Annual mean bottom-up methane fluxes for the eight sectors used to construct our a priori emissions for the year 2020.





#### 2.3 Background Mole Fractions

Methane observed at any location is a combination of local emissions and contributions transported from distant regions, commonly referred to as the background mole fraction. We calculate the modeled background mole fraction as two components: (1) contribution of methane mole fractions present at the endpoints of the particle trajectories - called the initial mole fraction, (2) contribution from the methane fluxes outside the study domain - from here onwards termed as boundary mole fractions. In our study, the transport modeling (see section 2.4) covers only 20 days backward from every observation. So the methane present in the atmosphere before that time is accounted for in the initial mole fraction. For generating initial mole fractions, we tested two global methane mole fraction products - CAMS global inversion-optimized greenhouse gas mole fractions, and the ECMWF Atmospheric Composition reanalysis EGG4, to identify the dataset that has the smaller bias relative to TROPOMI observations and thus provides a robust background for the inversion. The EGG4 dataset, which incorporates additional bias correction steps, demonstrated the smaller overall bias (mean bias error reduction of ~ 98% relative to CAMS data; MBE CAMS: -9.8 and MBE EGG4: 0.2) and was therefore adopted as the global initial mole fraction field. To account for uncertainties in the background, we applied a relative background error of 0.3% – 0.7% in the inversions, corresponding to the order of magnitude of the RMSD of EGG4 against TROPOMI (~5 ppb), and ensuring consistency between the assumed error and the observational bias characteristics.

## 2.4 Transport Modeling

This study uses the Lagrangian Particle Transport model - Flexpart v10.4 to calculate the sensitivity of the columnaveraged dry air methane mole fractions to the emission fluxes and background mole fractions. For this, the model is run in backward mode for 20 days from the time of the observations using ERA5 meteorology available at 0.5° x 0.5° resolution. The sensitivity of the simulated column at the receptor to emission fluxes is called Source-Receptor Relationship (SRR) [Seibert & Frank, 2004], and the sensitivity to the initial mole fraction field at the trajectory end points is called Background-Receptor Relationship (BRR). The SRRs and BRRs were calculated at 0.5° x 0.5° resolution for the study domain (5° to 38°N and 60° to 98°E) and at 2° x 2° globally, and include sensitivity reductions due to chemical reaction with the hydroxyl radical.

177 Methane mixing ratios can be modeled with Flexpart using:

$$y^{model} = Hf + H^{ini}y^{ini}$$
 (1)

where  $y^{model}$  is the model mole fraction, H is the sensitivity to emission fluxes (SRR), H<sup>ini</sup> is the sensitivity to initial mole fractions (BRR), f are the a priori fluxes, and  $y^{ini}$  are the background mole fractions. Here, the first term (Hf) is the contribution from fluxes to the modeled CH<sub>4</sub> total column, and the second term (H<sup>ini</sup> $y^{ini}$ ) is the contribution from the initial mole fraction. For modeling total column mixing ratios, Thompson et al. (2025) introduced an efficient framework that accounts for the averaging kernel used in the satellite retrieval. We follow their methodology and, thus, give only a short description. To compare the model and satellite retrievals, we need to consider the effect of the retrieval kernel on the model column mole fraction:

186 
$$X^{avg} = X^{pri} + \sum_{n=1}^{N} A_n (X_n^{model} - X_n^{pri}) w_n$$
 (2)





where  $X^{avg}$  is the model column average mole fraction,  $X^{pri}$  is the prior column mole fraction used in the satellite retrieval,  $A_n$  is the averaging kernel sensitivity at layer n,  $X_n^{model}$  is the model mole fraction at layer n,  $X_n^{pri}$  is the prior mole fraction at layer n,  $w_n$  is the pressure weighting term, and N is the total number of vertical layers used in the satellite retrieval. A total of 30000 particles were released per retrieval column. Inserting Eq. (1) into Eq. (2) leads to:

$$X^{avg} = X^{pri} + \sum_{n=1}^{N} A_n (H_n f + H_n^{ini} y_n^{ini} - X_n^{pri}) w_n$$
 (3)

Here, the term,  $\Sigma A_n H_n w_n$  is the total column SRR. The calculation of column SRRs relies on sampling particles in a grid cell and summing their contributions according to the retrieval layer from which they were released. While, in principle, one could retain information on the specific retrieval layer each particle originated from, Thompson et al. (2025) showed that this information can be incorporated more efficiently by carrying the product of the averaging kernel and pressure weight  $(A_n w_n)$  into the particle mass. This allows the number of particles released per layer to be varied according to  $P_n = PA_n w_n$ , where P is the total number of particles released per retrieval. Figure 5 illustrates a sample distribution, showing how the averaging kernel and pressure weighting determine the vertical distribution of particles across the retrieval layers. This formulation leads to a simplified expression equivalent to that used for point observations. The results are numerically consistent with the full layer calculation but require substantially less computation, making it possible to treat total column observations with the same efficiency as point measurements. More details on this method can be found in Thompson et al. (2025).

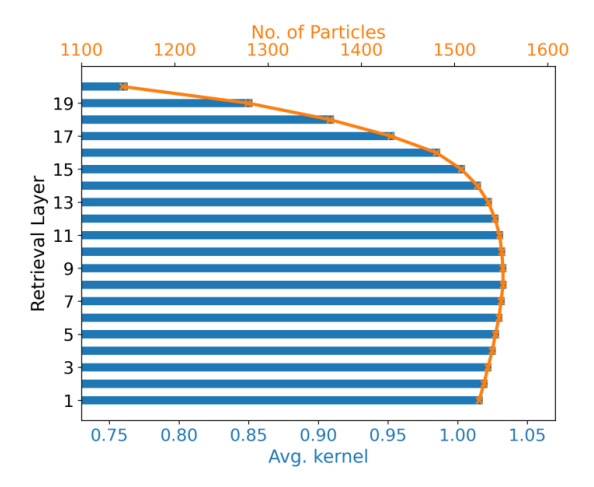


Figure 5. Vertical distribution of particles for a sample retrieval. Blue bars show the averaging kernel values for each retrieval layer, and the orange line indicates the corresponding number of particles released per layer after weighting by the averaging kernel and pressure term.

## 2.5 Inverse Modeling

The Bayesian inversion method [Tarantola, 2005] corrects the prior flux estimates based on the available observations, while accounting for uncertainties in both the measurements and the modeling system. This study employs the Bayesian inverse modeling system - Flexinvert [Thompson and Stohl, 2014] to optimize the methane emissions across South Asia. Here, we used the sensitivity fields derived from transport modeling to quantify the



214

215

216

217

219

220

221

222

223

224

225226

227

228

229

230

231

232

233

234

235

236

237

238

241



influence of surface emissions to the satellite-observed methane mole fractions, represented as the transport operator H. The inversion then adjusts the prior fluxes to minimize the mismatch between the modeled and observed mole fractions, resulting in posterior fluxes that are more consistent with the atmospheric measurements. This is formulated as a cost function J(x) that balances deviations from both prior emissions and observational constraints. The cost function is defined as:

218 
$$J(x) = \frac{1}{2} (x - x_b)^T B^{-1} (x - x_b) + \frac{1}{2} (y - Hx)^T R^{-1} (y - Hx)$$

where  $x_b$  is the state vector of prior fluxes, y is the observation vector, H is the transport operator, B and R are the error covariances associated with the prior errors and observation errors. The state vector is optimized at a 30-day temporal resolution and at spatial resolutions ranging from 0.5° to 2.0°, depending on how strongly emissions in a region influence the observations. The inversion was restricted to land regions, with only terrestrial fluxes being optimized. The state vector further contains scalar parameters for the initial mole fraction field. These are specified across four latitude bands (90°-30°N, 30°-0°N, 0°-30°S, and 30°-90°S) and three vertical layers (0-2000 m, 2000-10,000 m, and 10,000-50,000 m above ground level), and are optimized on a 30-day timescale. We used a range of prior and background uncertainties for the inversions (see section 3.1). For the reference inversion, a prior flux uncertainty of 100% and a background uncertainty of 0.3% are assumed. The prior error covariance matrix B is constructed by assigning the variance in each grid cell as the square of its prior uncertainty, while the covariances were defined using an exponential decay function with a correlation length of 250 km between grid cells. In addition, temporal correlations were accounted for using an exponential decay with a correlation timescale of 30 days. Observation errors were derived from the TROPOMI retrieval uncertainties. For each superobservation, the uncertainty was computed as the root-sum-square of the individual retrieval uncertainties, weighted by their respective ground pixel areas. The total observation space uncertainty includes both the superobservation error and the error from background mole fractions. This uncertainty corresponds to an IQR of 14-18 ppb with a mean of 16 ppb. The squares of these uncertainties were used as the variances in the observation error covariance matrix R. The errors in the super-observations were assumed to be uncorrelated. The cost function for the inversion can be solved either numerically or analytically. This study employs an analytical solution for inversions:

239 
$$x_a = x_b + (B^{-1} + H^T R^{-1} H)^{-1} H^T R^{-1} (y - H x_b)$$

where  $x_a$  is the posterior estimate.

### 3.1 Results and Discussion





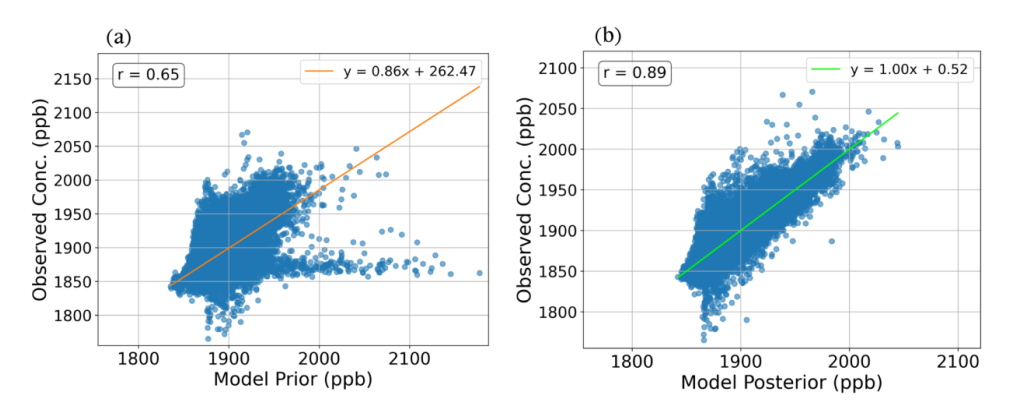


Figure 6. Scatter plot of observed TROPOMI CH<sub>4</sub> column-average mole fractions against FLEXPART model estimates over South Asia. The left figure shows results with prior and the right with posterior emissions.

Figure 6 shows the agreement between observed and modeled column-averaged methane mole fractions before and after the inversion. This plot gives a comprehensive view of the performance of the inversion system. The correlation coefficient increases from 0.65 (prior) to 0.89 (posterior), indicating a substantial improvement in the posterior estimates after assimilating the satellite observations. With the prior emissions, the slope between the model and the observations is 0.86 and there is a large positive intercept of 262 ppb. With the posterior emissions, the slope is close to 1 and the intercept nearly zero, indicating an almost unbiased fit. This validates that the posterior emissions better reproduce the observed atmospheric mole fractions, demonstrating the effectiveness of the inversion. However, since this validation is not against independent data, this shows only that the inversion is performing as expected.

The South Asian region experiences a distinct seasonal pattern characterized by wet summers and dry winters. During summer, from June to September, strong south-westerly winds prevail due to the South Asian monsoon, while winter is dominated by dry continental winds predominantly from the north-east.

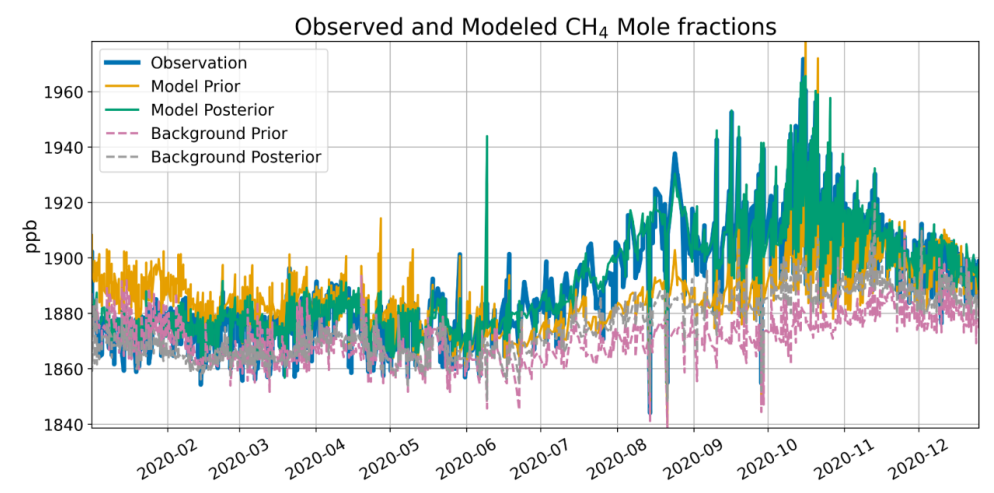


Figure 7. Time series of observed and modeled prior and posterior methane (CH<sub>4</sub>) column-averaged dry air mole fractions averaged over South Asia. Modeled prior and posterior background are also shown.





Figure 7 shows the time series of the spatially averaged observed and modeled column-average mole fractions of CH<sub>4</sub> for the reference inversion. The TROPOMI observations (blue line) show a strong increase in column-average CH<sub>4</sub> dry air mole fractions during and after the monsoon season. The prior background mole fractions (dashed purple line) are higher from October to February, due to the northerly winds carrying air which is enriched in CH<sub>4</sub>, and lower from June to September, due to the cleaner air arriving from the Southern Ocean during the monsoon season. Our inversion simultaneously optimizes both the background methane mole fractions and the prior emissions. The posterior background mole fractions (dashed grey line) are adjusted downward during January to May and upward from June. The model prior mole fractions (orange line) significantly overestimate the observations during the dry months from January to May and underestimate them during the wet period from June to September. The posterior mole fractions (green line) show the inversion's ability to bring the simulated values closer to the observations. While this is partly due to a correction of the background values, a substantial portion of the correction is due to increased emission contributions from South Asia during June to September (Fig. 10). These results indicate that the bottom-up inventories misrepresent the seasonal dynamics of methane emissions in South Asia.

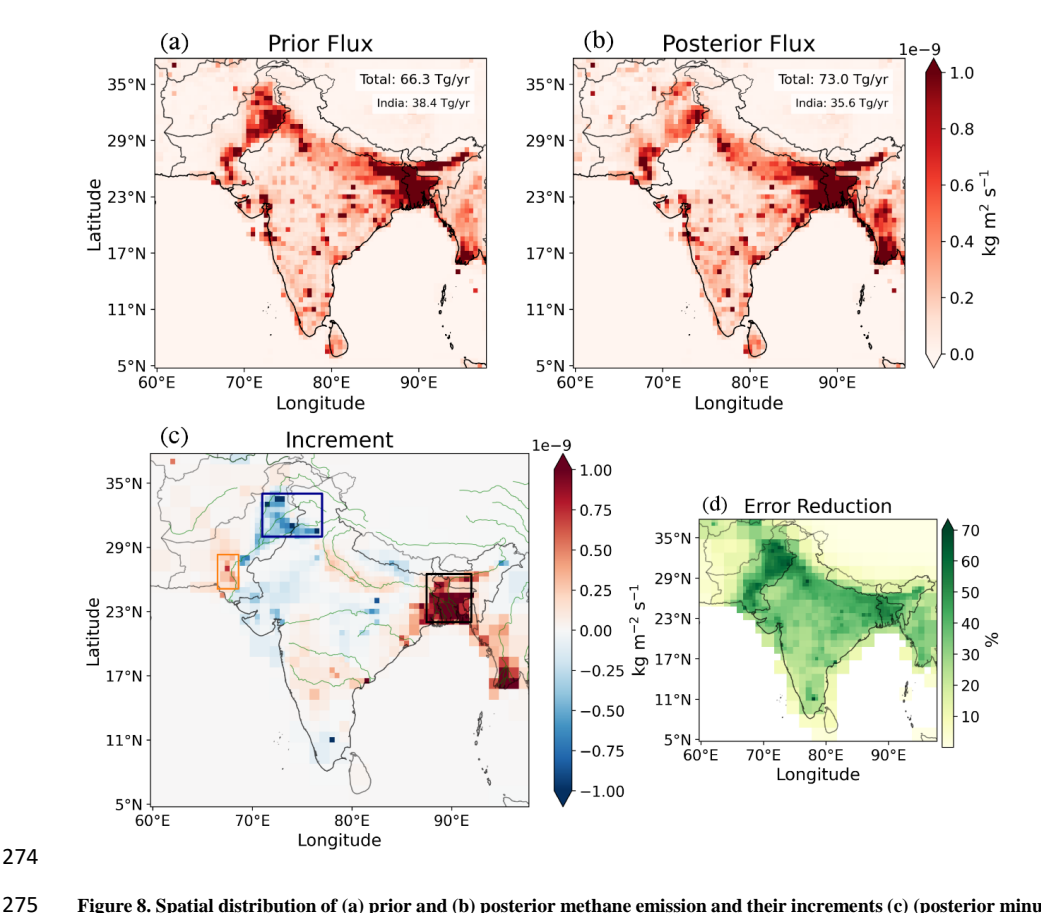


Figure 8. Spatial distribution of (a) prior and (b) posterior methane emission and their increments (c) (posterior minus prior) across South Asia for the year 2020. Positive values (red) indicate regions where emissions were underestimated in the prior inventories, while negative values (blue) indicate overestimation. The three marked boxes highlight regions





of interest discussed in the text. Major river systems (Indus, Ganges, and others) are overlaid in green for geographical context. (d) shows the uncertainty reduction across the region.

Figure 8 (a)-(b) shows the spatial distribution of the prior and posterior methane fluxes and Table 2 provides a summary of the methane emissions for the different countries. The prior methane emissions from South Asia as a whole are  $66.34 \pm 2.58$  Tg yr<sup>-1</sup>, with the top three emitters India, Bangladesh and Pakistan contributing  $38.41 \pm 2.54$ ,  $7.57 \pm 0.36$ , and  $8.00 \pm 0.22$  Tg yr<sup>-1</sup>, respectively. The countries Afghanistan, Bhutan, Sri Lanka and Nepal (referred to as ABSN from here onwards) together contribute only 2.04 Tg yr<sup>-1</sup>. Myanmar, which is only partially in our inversion domain, contributes a total of 10.3 Tg yr<sup>-1</sup>.

The inversion gives a total posterior methane flux of  $73.01 \pm 0.53$  Tg yr<sup>-1</sup>, 6.7 Tg yr<sup>-1</sup> more than the prior estimate. Of this, India accounts for  $35.62 \pm 0.47$  Tg yr<sup>-1</sup> (a reduction of 7% from the prior), Bangladesh for  $13.16 \pm 0.19$  Tg yr<sup>-1</sup> (an increase of 74%) and Pakistan for  $6.55 \pm 0.09$  Tg yr<sup>-1</sup> (a reduction of 18%), respectively. Bangladesh accounts for the majority of the regional increase. The posterior emissions from ABSN countries, 2.30 Tg yr<sup>-1</sup> (an increase of 13%) remain relatively minor.

Region	Prior Emissions (Tg yr <sup>-1</sup> )	Posterior Emissions (Tg yr <sup>-1</sup> )	Absolute Change (Tg yr <sup>-1</sup> )	Relative Change (%)
India	$38.41 \pm 2.54$	$35.62 \pm 0.47$	-2.79	-7.3%
Bangladesh	$7.57 \pm 0.36$	$13.16 \pm 0.19$	+5.60	+74%
Pakistan	$8.00 \pm 0.22$	$6.55 \pm 0.09$	-1.45	-18.1%
Afghanistan	$0.61 \pm 0.02$	$1.07 \pm 0.01$	+0.46	+75.4%
Bhutan	0.03	0.03	0	0%
Sri Lanka	$0.50 \pm 0.03$	$0.56 \pm 0.02$	+0.06	12%
Nepal	$0.90 \pm 0.06$	$0.65 \pm 0.03$	-0.25	-27.8%
Others	$10.32 \pm 0.22$	$15.38 \pm 0.14$	+5.06	+49%
Total	<b>66.34</b> ± 2.58	<b>73.01</b> ± 0.53	+6.67	+10%

Table 2. Prior and posterior methane emission estimates (Tg yr $^{-1}$  CH $_4$ ) for South Asia and individual countries in 2020. The inversion increases the regional total from  $66.34 \pm 2.58$  Tg yr $^{-1}$  to  $73.01 \pm 0.53$  Tg yr $^{-1}$ , with the largest upward adjustment over Bangladesh (+5.6 Tg yr $^{-1}$ ), while India shows a reduction of -2.8 Tg yr $^{-1}$ . Smaller contributions come from Afghanistan, Bhutan, Sri Lanka, and Nepal (ABSN).

Figure 8 (c) shows the spatial distribution of the increments in the methane fluxes after the inversion (posterior prior) overlaid with major rivers in the region. Areas dominated by wetlands and agriculture (Fig. 4, Sup. Fig. 1) show the strongest posterior-prior differences. The majority of these positive increments were observed in the eastern Indo-Gangetic Plain and Bangladesh. This region, marked with a black box (22–26.5°N, 87.5–92°E) in Fig. 8(c), alone has a posterior emission of 20.83 Tg yr<sup>-1</sup> of methane, an increase of +8.4 Tg yr<sup>-1</sup> from prior emissions, indicating that inventories substantially underestimate emissions in these densely irrigated and wetland-rich areas. This is a region of focus in our study and detailed analysis is done later on in this section. The

https://doi.org/10.5194/egusphere-2025-5108 Preprint. Discussion started: 14 November 2025 © Author(s) 2025. CC BY 4.0 License.



306

307

308

309

310

311

312

313

314

315

316 317

318

319

320

321

322

323

324

325

326

327

328

329

330

331

332

333



positive increments in the north-western India clearly align with the trajectory of the river Yamuna and Ganges, indicating uncaptured emissions in inventories, possibly from the agriculture sector. Several studies have shown rice cultivation as a key contributor to methane emissions here due to the use of nitrogen fertilizers, organic manure, and livestock population in this region [Singh et al., 2021].

Most of the negative adjustments are seen over western India and Pakistan. A comparison with the prior flux maps (Fig. 4) shows that these are mostly agricultural and waste-related emissions in the prior (Sup. Fig. 1). In the area marked within the blue box, emission estimates are reduced by -2.4 Tg yr<sup>-1</sup>, suggesting that bottom-up inventories overestimate fluxes in these sparsely monitored regions. While the total methane emissions in Pakistan decrease overall after the inversion, the region (marked with an orange box) within the Lower Indus Basin (LIB) shows an increase of 0.5 Tg yr<sup>-1</sup>. A closer examination at this region reveals that, when the prior fluxes show an almost flat seasonal cycle, the posterior fluxes capture a distinct seasonality with peaks in May and August (Fig. 9(b)). This region is periodically wetted by the Indus River, whose flow is governed by both natural processes—such as glacier and snowmelt from the northern mountains and monsoonal rainfall—and strong human regulation through irrigation and agricultural diversions, particularly within the LIB. Previous studies, such as Baig et al. (2022), have also reported a comparable dual-peak seasonality in river discharge in the Upper Indus Basin (UIB), driven by glacier melt, snow and rainfall contributions. To examine this further, we analyzed runoff data from ERA5-Land [Muñoz-Sabater et al., 2021], which combine surface and subsurface components resulting from rainfall, melting snow, and soil drainage. The analysis reveals a strikingly similar spatial pattern in annual runoff (Fig. 9(a)) to the flux increments seen in the orange-box region. The runoff data also exhibit a dual-peak cycle in the UIB, with maxima in June and September, while the lower Indus Basin shows only a single pronounced peak in August (Fig. 9(b)). This difference likely reflects the strong influence of the Indus Basin Irrigation System, where extensive human regulation and diversion for irrigation and agriculture modify the natural water flow (Janjua et al., 2021), a process that may not be represented accurately in the river flow datasets (Liu et al., 2018). The posterior methane fluxes in Fig. 9(b) tend to peak slightly earlier than the corresponding runoff peaks, indicating a temporal lag between runoff data and methane emissions. This may be due to known uncertainties in Indus discharge data, where mean annual biases of about 22% and monthly errors exceeding 200% have been reported (Liu et al., 2018), potentially distorting both the timing and magnitude of seasonal peaks. Such discrepancies are further amplified downstream by barrage operations and canal withdrawals in the Indus Basin Irrigation System (Bhatti et al., 2019), while long-term analyses also indicate a progressive shift toward earlier streamflow timing (Ali et al., 2023). Further, the grid cell corresponding to Karachi, Pakistan, also shows a positive increment, with the highest posterior CH<sub>4</sub> emissions occurring in September. Interestingly, this coincides with record monsoonal rainfall that caused severe flooding in Karachi during late August 2020.





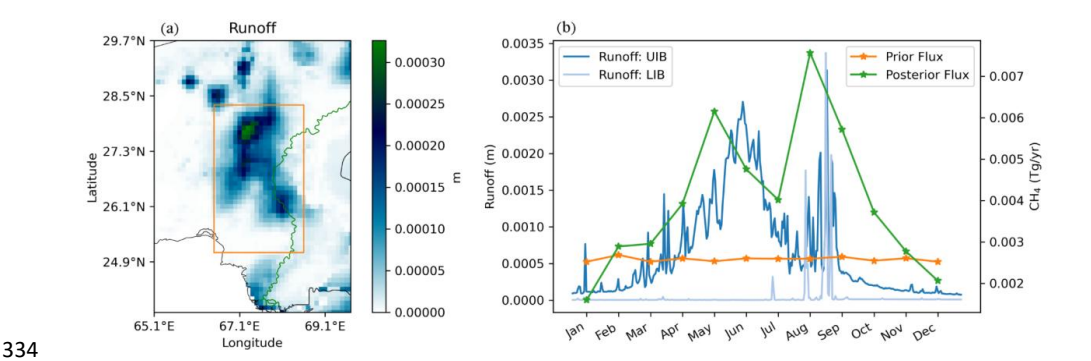


Figure 9. (a) Spatial distribution of annual runoff from ERA5-Land in the Lower Indus Basin (LIB), with the orange box indicating the analysis area. (b) Monthly methane fluxes (prior in orange, posterior in green) in the LIB compared with runoff time series for both the upper and lower Indus Basin. The posterior fluxes capture a clear seasonal cycle with peaks in May and August, consistent with runoff variability, showing a similar pattern to runoff variability in the basin.

The year 2020 marked an above-normal monsoonal rainfall in South Asia, with India receiving 109% of its Long Period Average (LPA). This marked the second consecutive year of above-normal monsoon rainfall in India, following 2019's 110% of LPA - a pattern not observed since 1958 and 1959. Concurrently, Bangladesh faced historic flooding, with approximately a quarter of the country submerged. Almost a million homes were inundated, and more than 1,500 square kilometers of farmland were damaged across the country.

To understand the role of the monsoon in the emissions, their key natural drivers such as rainfall and soil moisture were compared with monthly prior and posterior methane fluxes. Rainfall data is taken from the Global Precipitation Climatology Project [Adler et al., 2019] and soil wetness from ERA5-Land [Hersbach et al., 2018], with the top four layers (~3 m depth) averaged. Figure 10 shows prior and posterior fluxes alongside rainfall and soil wetness for the South Asia full domain (top) and the Bangladesh-focused black box region (bottom). The figure highlights a strong seasonal contrast. During the early part of the year (Jan–May), the inversion reduced fluxes by 46% relative to the prior (10.5 Tg yr<sup>-1</sup>). In the monsoon months (Jun–Sep), posterior fluxes showed a 70% upward adjustment (19.3 Tg yr<sup>-1</sup>), coinciding with peak rainfall and soil wetness, and reflecting the strong hydrological forcing on emissions (Sup. Fig.2). The largest increments occur in July–August, when rainfall and soil wetness reach their maxima. In the post-monsoon period (Oct–Dec), posterior emissions were 13% lower than the prior (2 Tg yr<sup>-1</sup>), with the retreat of rainfall and soil saturation. The seasonal amplitude is strongest within the box region, consistent with the historic flooding in Bangladesh.





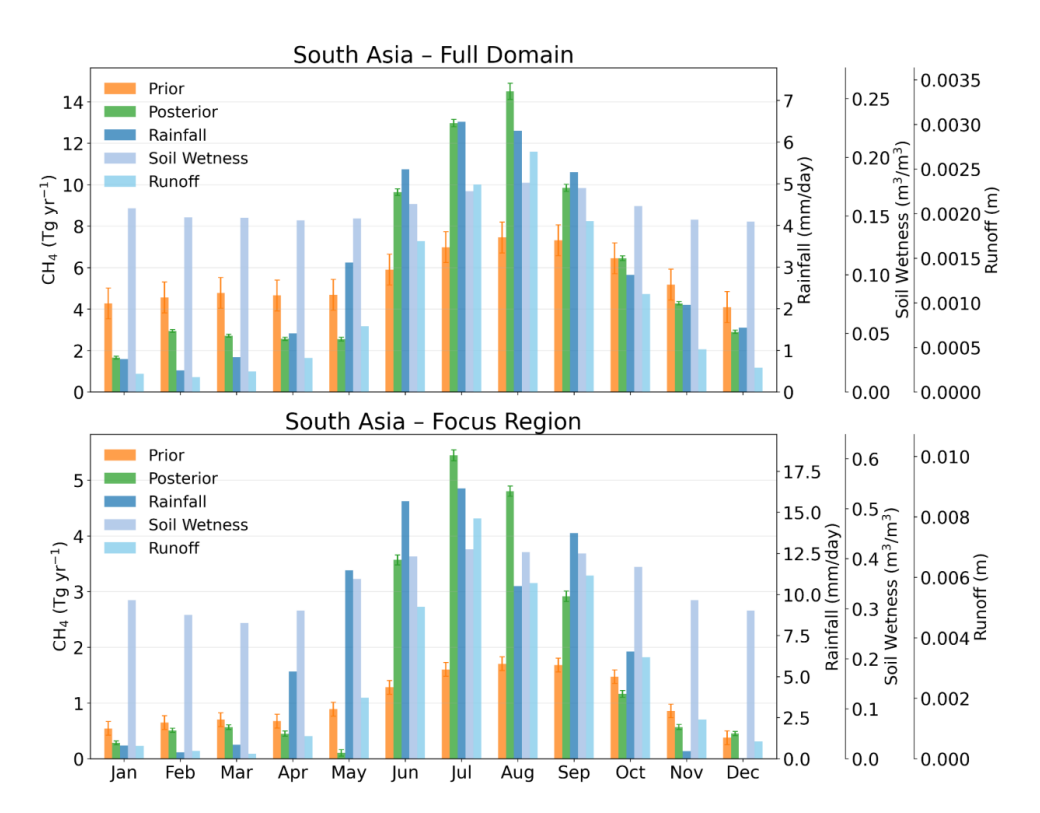


Figure 10. Monthly prior (blue) and posterior (orange) methane fluxes for the full South Asia domain (top) and the Bangladesh focus region (bottom), shown together with monthly mean rainfall, runoff and soil wetness.

To assess this link statistically, we calculated the spatio-temporal Pearson correlation of methane fluxes before and after the inversion with the hydrological drivers. This analysis revealed that soil wetness shows a correlation of 0.28 with the prior fluxes, which increases to 0.31 after inversion, corresponding to a 25% rise in the explained variance. For rainfall, the correlation increases from 0.48 to 0.53 (+22% in explained variance). The rainfall correlation was calculated with a one-month lag to reflect the delayed response of emissions to precipitation-induced inundation. The relationship with runoff strengthens from 0.23 in the prior to 0.32 in the posterior fluxes - an increase of about 94% in the variance explained. Together, these results indicate a systematic enhancement in the linear relationship between the posterior methane fluxes and hydrological variability.

Thus, it seems that the strong South Asian monsoon and associated extensive flooding were at least partly causal in driving our positive flux increments in this region. Studies such as Peng et al. (2022) identified wetland emissions as the major reason for the 2020 global methane growth. According to NASA Earth Observatory (2022), half of the surge in atmospheric methane in 2020 was driven by wetland emissions. Fueled by the strong South Asian monsoon in 2020, wetlands in Bangladesh and possibly all of South Asia appear to have contributed substantially to this global increase. Niwa et al. (2025), also emphasized that wetlands and agricultural activities are key drivers of biogenic methane emissions in this region, substantially contributing to the global methane increase observed from 2020 to 2022. These regions of spatial mismatch between prior and posterior fluxes would





be of prime interest for targeted field campaigns or improved process models (hydrology, rice paddies) to effectively reduce inventory uncertainty.

An uncertainty reduction map is calculated as one minus the ratio of posterior to prior uncertainties (Fig. 8 (d)). The inversion could achieve a maximum of 70% uncertainty reduction in some regions with a median uncertainty reduction close to 40% in most of the area. The maximum uncertainty reduction is mostly achieved in the regions with higher emissions and higher data coverage.

#### 3.2 Ensemble of Inversions

To quantify the sensitivity of our inversion to the uncertainty assumptions, we performed nine inversions combining three levels of prior flux uncertainty (50 %, 100 %, 200 %) with three background error settings (0.3%, 0.5%, 0.7%). Posterior fluxes for South Asia range from 65.16 to 74.62 Tg yr<sup>-1</sup>, with an ensemble mean of 70.97 Tg yr<sup>-1</sup>, a standard deviation of 3.16 Tg yr<sup>-1</sup>, and an ensemble spread of 9.46 Tg yr<sup>-1</sup> (~13 % of the mean), illustrating the uncertainty introduced by our prior choices (Fig. 11). For the simulations with the lowest prior uncertainty (50%) and the highest prior uncertainty (200%), increasing the background error from 0.3% to 0.7% reduces the posterior fluxes, whereas for the simulations with the moderate prior uncertainty (100%), posterior fluxes show a slight increase from 73.0 to 73.8 Tg yr<sup>-1</sup>, but are remarkably stable (<1 Tg yr<sup>-1</sup> change). This demonstrates a robust solution under moderate changes of a-priori background uncertainty.

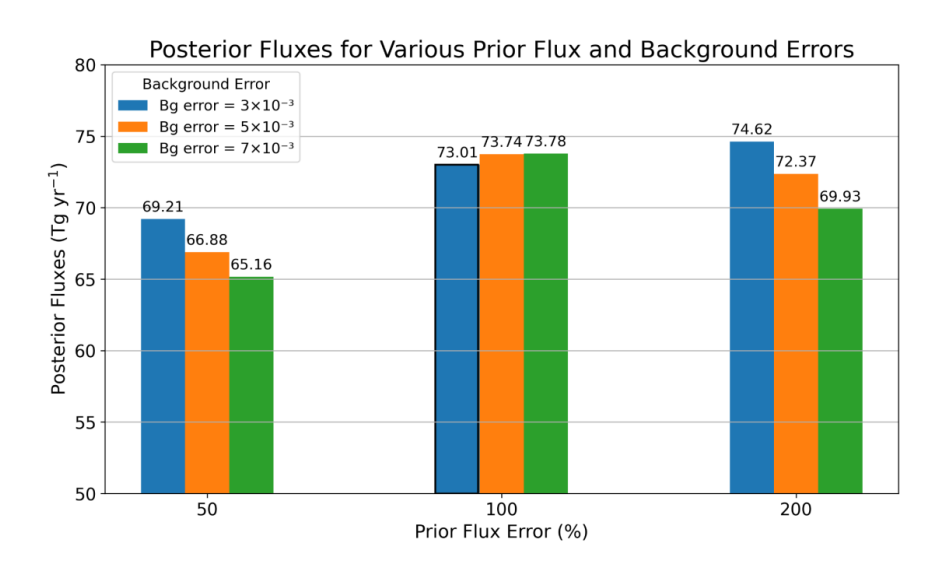


Figure 11. Posterior CH4 flux estimates as a function of prior-flux uncertainty (50 %, 100 %, 200 %) and three background-error settings (0.3% in blue, 0.5% in orange, 0.7% in green). The reference inversion is indicated with a black outline.

Figure 12 presents the monthly ensemble means of posterior fluxes compared with the priors, with the error bars  $(\pm 1 \sigma)$  indicating one-sigma spread across the nine inversion experiments. The darker shaded bars correspond to the full South Asia domain, while lighter shades represent the Bangladesh focus region. Across all ensembles, the posterior fluxes exhibit a consistent and robust seasonal cycle. Posterior flux adjustments are negative during





January to May and again in October to December. The ensemble spread remains very small during this period, when the number of TROPOMI observations is large (Fig. 3). In contrast, June to September shows strong positive increments, particularly in the Bangladesh focus region where posterior fluxes nearly triple the priors, reflecting the severe flooding and widespread wetland inundation. The ensemble spread is largest during June to August, reaching  $\pm 2$  Tg yr<sup>-1</sup> for the full domain and  $\pm 0.8$  Tg yr<sup>-1</sup> for the focus region, coinciding with reduced satellite coverage under cloudy monsoon conditions. Importantly, the increments are not only consistent in time but also across space, with all ensemble members showing a coherent increase in emissions over the same regions. The persistence of these adjustments across all ensemble members highlights the robustness of the inversion in capturing the influence of the South Asian monsoon and hydrology on methane emissions.

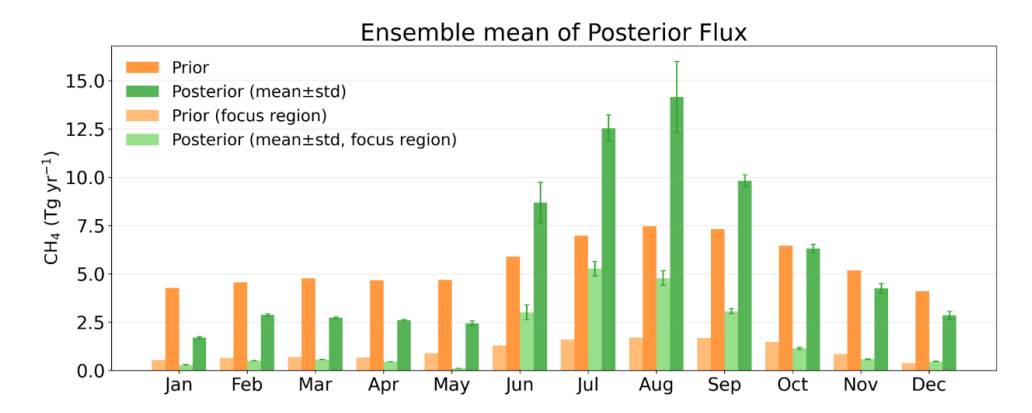


Figure 12. Ensemble mean monthly CH<sub>4</sub> fluxes (Tg yr<sup>-1</sup> CH<sub>4</sub>), showing prior estimates (orange) and posterior means (green) with  $\pm 1~\sigma$  error bars across nine inversion experiments.

### 4. Conclusion

This study demonstrates the value of assimilating TROPOMI satellite observations into a Bayesian inversion framework to constrain regional methane emissions over South Asia. The inversion substantially improves the agreement between observed and modeled mole fractions, as seen by the increase in correlation from 0.65 to 0.89 and the shift toward an unbiased fit. Posterior fluxes reveal substantial underestimations in the inventories over wetland-rich and intensively cultivated regions like eastern India and Bangladesh as well as in the Indus river basin. The inversion estimates a total of 73.0 Tg yr<sup>-1</sup> CH<sub>4</sub> emissions for South Asia in 2020, which is 6.7 Tg yr<sup>-1</sup> higher than the prior estimate. Within this increase, Bangladesh alone contributes +5.6 Tg yr<sup>-1</sup>, while the blackbox region covering eastern India and Bangladesh accounts for +8.4 Tg yr<sup>-1</sup> of the regional increment. In contrast, western India and northern Pakistan show negative adjustments, suggesting overestimation of fluxes in the prior inventories. However, a localized region within the Lower Indus Basin shows a notable positive increment (~0.5 Tg yr<sup>-1</sup>), with the posterior fluxes capturing a distinct dual-peak seasonality (May and August) absent in the prior estimates. This enhanced seasonality coincides with the runoff cycle of the Indus River, which is modulated by both glacier and snowmelt from the Upper Indus and by monsoonal rainfall and irrigation in the lower basin.

Importantly, the prior emissions overestimate methane during the early part of the year (January–May, by 46%) as well as during November-December (by 13%), while underestimating it during June–September (by 70%) - a





428	seasonal mismatch corrected by the inversion. Most of the spatial and temporal corrections coincide with the
429	regions of heavy monsoonal rainfall. Further analysis shows increased correlation between posterior fluxes and
430	key environmental drivers like precipitation, soil moisture, and runoff. These analyses suggest that the 2020 rise
431	in methane emissions is strongly linked to biogenic processes driven by glacial melt (in the Indus river basin),
432	heavy monsoonal rainfall and enhanced inundation (both in the Indus river basin and in Bangladesh). These
433	findings are consistent with earlier studies (e.g., Peng et al., (2022), Niwa et al., (2025)) that identify wetlands and
434	agriculture as dominant contributors to the regional and global methane budget in recent years. However,
435	inventories do not reproduce the important seasonal variability of emissions in the large river systems - a finding
436	that may apply also to other regions than South Asia.
437	A nine-member ensemble of inversions provides a robust sensitivity analysis, quantifying the spread introduced
438	by varying prior flux and background mole fraction errors. The posterior emissions vary within a ~9.5 Tg yr
439	range, with the most stable results achieved under moderate a priori uncertainty (100%). Seasonal patterns in all
440	posterior ensembles show enhanced emissions during the monsoon months. The spread across ensemble members
441	was low during the dry months, indicating robust agreement when observational coverage was sufficient. The
442	ensemble results highlight the critical role of prior uncertainty settings in inverse modeling and demonstrate the
443	necessity of ensemble approaches for deriving robust uncertainty estimates. Overall, this work provides a refined
444	top-down constraint on South Asia's methane emissions for the year 2020 and highlights key spatial and seasonal
445	discrepancies in existing inventories, offering guidance for future improvements in emission reporting and
446	process-based modeling.
447	Code and Data availability
448	The TROPOMI/WFMD methane retrievals and documentation are publicly available from the University of
449	Bremen: <a href="https://www.iup.uni-bremen.de/carbon_ghg/products/tropomi_wfmd/">https://www.iup.uni-bremen.de/carbon_ghg/products/tropomi_wfmd/</a> . The source codes for the
450	FLEXPART Lagrangian transport model and the FLEXINVERT Bayesian inversion system used in this study
451	can be accessed through the GitLab repository: <a href="https://git.nilu.no/flexpart">https://git.nilu.no/flexpart</a> .
452	Author contribution
453	Conceptualization: Andreas Stohl, Rakesh Subramanian
454	Data curation: Rakesh Subramanian
455	Formal analysis: Rakesh Subramanian
456	Funding acquisition: Andreas Stohl
457	Investigation: Rakesh Subramanian
458	Methodology: Rakesh Subramanian, Rona Thompson, Andreas Stohl
459	Resources: Martin Vojta, Rona Thompson, Oliver Schneising
460	Supervision: Andreas Stohl, Rona Thompson
461	Validation: Rakesh Subramanian
462	Visualization: Rakesh Subramanian
463	Writing (original draft preparation): Rakesh Subramanian





- 464 Writing (review and editing): Rakesh Subramanian, Andreas Stohl, Rona Thompson, Martin Vojta, Oliver
- 465 Schneising

### 466 Acknowledgements

- 467 This work was funded internally by the University of Vienna as part of the Vienna Network for Atmospheric
- 468 Research (VINAR). Algorithm development partly benefited from the project GHG-KIT (Keep it traceable -
- 469 Prototyping a satellite-enabled, independent tool-kit system for GHG verification in Austria) funded by the
- 470 Austrian Research Promotion Agency (FFG) under contract FO999893432.
- 471 R. L. Thompson received financial support from the REGAME project funded by the Research Council of Norway
- 472 (grant no. 325610), which also supported some of the work at the University of Vienna.
- 473 University of Bremen contributions received funding from the European Space Agency (ESA) via the projects
- 474 GHG-CCI+ and MethaneCAMP (ESA contract nos. 4000126450/19/I-NB and 4000137895/22/I-AG) and from
- 475 the Federal Ministry of Research, Technology and Space (BMFTR) within its project ITMS via grant no. 01
- 476 LK2103A. The TROPOMI/WFMD retrievals were performed on HPC facilities of the IUP, University of Bremen,
- funded under DFG/FUGG grant nos. INST 144/379-1 and INST 144/493-1.
- 478 This publication contains modified Copernicus Sentinel data (2020). Sentinel-5 Precursor is an ESA mission
- 479 implemented on behalf of the European Commission. The TROPOMI payload is a joint development by the ESA
- 480 and the Netherlands Space Office (NSO). The Sentinel-5 Precursor ground-segment development has been funded
- by the ESA and with national contributions from the Netherlands, Germany, and Belgium.

## 482 References

- 483 Adler, R., Wang, J.-J., Sapiano, M., Huffman, G., Bolvin, D., Nelkin, E., and NOAA CDR Program: Global
- 484 Precipitation Climatology Project (GPCP) Climate Data Record (CDR), Version 1.3 (Daily), NOAA National
- 485 Centers for Environmental Information, <a href="https://doi.org/10.7289/V5RX998Z">https://doi.org/10.7289/V5RX998Z</a>.
- 486 Ali, S., Kim, B.-H., Akhtar, T., and Kam, J.: Past and future changes toward earlier timing of streamflow over
- 487 Pakistan from bias-corrected regional climate projections (1962-2099), J. Hydrol., 617, 128959,
- 488 https://doi.org/10.1016/j.jhydrol.2022.128959, 2023.
- 489 Baig, S., Sayama, T., and Yamada, M.: Quantifying the changes in the runoff and its components across the Upper
- 490 Indus River Basin under climate change, J. Water Clim. Change, 13, 3416-3434,
- 491 https://doi.org/10.2166/wcc.2022.153, 2022.
- 492 Belikov, D. A., Patra, P. K., Terao, Y., Naja, M., Ahmed, M. K., and Saitoh, N.: Assessment of the impact of
- 493 observations at Nainital (India) and Comilla (Bangladesh) on the CH4 flux inversion, Prog. Earth Planet. Sci., 11,
- 494 36, https://doi.org/10.1186/s40645-024-00634-x, 2024.
- 495 Bhatti, M. T., Anwar, A. A., and Shah, M. A. A.: Revisiting Telemetry in Pakistan's Indus Basin Irrigation System,
- 496 Water, 11, 2315, <a href="https://doi.org/10.3390/w11112315">https://doi.org/10.3390/w11112315</a>, 2019.





- 497 Bloom, A. A., Bowman, K. W., Lee, M., Turner, A. J., Schroeder, R., Worden, J. R., Weidner, R. J., McDonald,
- 498 K. C., and Jacob, D. J.: CMS: Global 0.5-deg Wetland Methane Emissions and Uncertainty (WetCHARTs v1.3.3),
- 499 ORNL DAAC, Oak Ridge, Tennessee, USA, <a href="https://doi.org/10.3334/ORNLDAAC/1502">https://doi.org/10.3334/ORNLDAAC/1502</a>, 2024.
- 500 Colligan, T., Poulter, B., and Quinn, C.: LPJ-EOSIM L2 Global Simulated Monthly Wetland Methane Flux V001,
- 501 NASA EOSDIS Land Processes Distributed Active Archive Center (LP DAAC), 2024. Available at:
- https://doi.org/10.5067/Community/LPJ-EOSIM/LPJ\_EOSIM\_L2\_MCH4E.001.
- 503 Crippa, M., Guizzardi, D., Pagani, F., Banja, M., Muntean, M., Schaaf, E., Becker, W., Monforti-Ferrario, F.,
- 504 Quadrelli, R., Risquez Martin, A., Taghavi-Moharamli, P., Köykkä, J., Grassi, G., Rossi, S., Brandao De Melo,
- 505 J., Oom, D., Branco, A., San-Miguel, J., and Vignati, E.: GHG emissions of all world countries, Publications
- Office of the European Union, Luxembourg, 2023, <a href="https://doi.org/10.2760/953322">https://doi.org/10.2760/953322</a>, JRC134504.
- 507 Copernicus Atmosphere Monitoring Service (CAMS): CAMS global greenhouse gas reanalysis (EGG4),
- 508 ECMWF, 2021. Available at: https://ads.atmosphere.copernicus.eu/datasets/cams-global-ghg-reanalysis-egg4
- 509 Deng, Z., Ciais, P., Tzompa-Sosa, Z. A., Saunois, M., Qiu, C., Tan, C., Sun, T., Ke, P., Cui, Y., Tanaka, K., Lin,
- 510 X., Thompson, R. L., Tian, H., Yao, Y., Huang, Y., Lauerwald, R., Jain, A. K., Xu, X., Bastos, A., Sitch, S.,
- 511 Palmer, P. I., Lauvaux, T., d'Aspremont, A., Giron, C., Benoit, A., Poulter, B., Chang, J., Petrescu, A. M. R.,
- 512 Davis, S. J., Liu, Z., Grassi, G., Albergel, C., Tubiello, F. N., Perugini, L., Peters, W., and Chevallier, F.:
- 513 Comparing national greenhouse gas budgets reported in UNFCCC inventories against atmospheric inversions,
- Earth Syst. Sci. Data, 14, 1639–1675, <a href="https://doi.org/10.5194/essd-14-1639-2022">https://doi.org/10.5194/essd-14-1639-2022</a>, 2022.
- 515 Doubalova, J. and Sindelarova, K.: Gridded CH4 emissions from termites, Copernicus Atmosphere Monitoring
- 516 Service Report, CAMS81\_2017SC1\_D81.3.4.1-201808\_v1, 2018. Available at:
- 517 https://atmosphere.copernicus.eu/sites/default/files/2019-11/26\_CAMS81\_2017SC1\_D81.3.4.1-
- 518 <u>201808\_v1\_APPROVED\_Ver1.pdf</u>.
- Etiope, G., Ciotoli, G., Schwietzke, S., and Schoell, M.: Gridded maps of geological methane emissions and their
- 520 isotopic signature, Earth Syst. Sci. Data, 11, 1–22, https://doi.org/10.5194/essd-11-1-2019, 2019.
- 521 Ganesan, A. L., Bousquet, P., Ciais, P., Broquet, G., Roche, M., Darras, S., and Granier, C.: Atmospheric
- 522 observations show accurate reporting and little growth in India's methane emissions, Nat. Commun., 8, 836,
- 523 <u>https://doi.org/10.1038/s41467-017-00994-7</u>, 2017.
- 524 Garg, A., Shukla, P. R., and Kapshe, M.: The sectoral trends of multigas emissions inventory of India, Atmos.
- 525 Environ., 40, 4608–4620, https://doi.org/10.1016/j.atmosenv.2006.03.045, 2006.
- 526 Granier, C., Darras, S., Denier van der Gon, H., Doubalova, J., Elguindi, N., Galle, B., Gauss, M., Guevara, M.,
- 527 Jalkanen, J.-P., Kuenen, J., Liousse, C., Quack, B., Simpson, D., and Sindelarova, K.: The Copernicus Atmosphere
- 528 Monitoring Service global and regional emissions (April 2019 version), Copernicus Atmosphere Monitoring
- 529 Service (CAMS) Report, 2019. Available at: <a href="https://doi.org/10.24380/d0bn-kx16">https://doi.org/10.24380/d0bn-kx16</a>.





R., Rozum, I., Schepers, D., Simmons, A., Soci, C., Dee, D., and Thépaut, J.-N.: ERA5 hourly data on single levels from 1940 to present, Copernicus Climate Change Service (C3S) Climate Data Store (CDS), 2018.

Available at: <a href="https://cds.climate.copernicus.eu/datasets/reanalysis-era5-single-levels">https://cds.climate.copernicus.eu/datasets/reanalysis-era5-single-levels</a>

https://doi.org/10.24381/cds.adbb2d47.

Hersbach, H., Bell, B., Berrisford, P., Biavati, G., Horányi, A., Muñoz Sabater, J., Nicolas, J., Peubey, C., Radu,

- Ito, A., Patra, P. K., and Umezawa, T.: Bottom-up evaluation of the methane budget in Asia and its subregions,
   Global Biogeochem. Cycles, 37, e2023GB007723, <a href="https://doi.org/10.1029/2023GB007723">https://doi.org/10.1029/2023GB007723</a>, 2023.
- Janardanan, R., Maksyutov, S., Tsuruta, A., Wang, F., Tiwari, Y. K., Valsala, V., Ito, A., Yoshida, Y., Kaiser, J.
- W., and Janssens-Maenhout, G.: Country-Scale Analysis of Methane Emissions with a High-Resolution Inverse
- Model Using GOSAT and Surface Observations, Remote Sens., 12, 375, <a href="https://doi.org/10.3390/rs12030375">https://doi.org/10.3390/rs12030375</a>,
- 540 2020
- 541 Jan-jua, S., Hassan, I., Muhammad, S., Ahmed, S., and Ahmed, A.: Water management in Pakistan's Indus Basin:
- 542 challenges and opportunities, Water Pol., 23, 1329–1343, https://doi.org/10.2166/wp.2021.068, 2021.
- 543 Liu, J., Kang, S., Hewitt, K., Hu, L., Xianyu, L., and others: Large observational bias on discharge in the Indus
- Five since 1970s, Sci. Rep., 8, 17291, https://doi.org/10.1038/s41598-018-35600-3, 2018.
- 545 Ministry of Earth Sciences, Government of India: Salient Features of Monsoon 2020, Press Information Bureau,
- 1 October 2020. Available at: <a href="https://www.pib.gov.in/Pressreleaseshare.aspx?PRID=1660645">https://www.pib.gov.in/Pressreleaseshare.aspx?PRID=1660645</a>.
- 547 Ministry of Environment, Forest and Climate Change (MoEFCC), Government of India: First Biennial Update
- 548 Report to the United Nations Framework Convention on Climate Change, 2016. Available at:
- 549 <u>https://unfccc.int/documents/180646</u>.
- 550 Ministry of Environment, Forest and Climate Change (MoEFCC), Government of India: Second Biennial Update
- 551 Report to the United Nations Framework Convention on Climate Change, 2018. Available at:
- 552 <a href="https://unfccc.int/documents/192316">https://unfccc.int/documents/192316</a>.
- 553 Ministry of Environment, Forest and Climate Change (MoEFCC), Government of India: Third Biennial Update
- 554 Report to the United Nations Framework Convention on Climate Change, 2021. Available at:
- 555 <a href="https://unfccc.int/documents/268470">https://unfccc.int/documents/268470</a>.
- 556 Ministry of Environment, Forest and Climate Change (MoEFCC), Government of India: Fourth Biennial Update
- 557 Report to the United Nations Framework Convention on Climate Change, 2024. Available at:
- 558 <u>https://unfccc.int/documents/645149</u>.
- 559 Ministry of Environment, Forest and Climate Change (MoEFCC), Government of India: India's Third National
- 560 Communication and Initial Adaptation Communication to the United Nations Framework Convention on Climate
- Change, 2023. Available at: <a href="https://unfccc.int/sites/default/files/resource/India-TNC-IAC.pdf">https://unfccc.int/sites/default/files/resource/India-TNC-IAC.pdf</a>.





- 562 Muñoz-Sabater, J., Dutra, E., Agustí-Panareda, A., Albergel, C., Arduini, G., Balsamo, G., Boussetta, S., Choulga,
- 563 M., Harrigan, S., Hersbach, H., Martens, B., Miralles, D. G., Piles, M., Rodríguez-Fernández, N. J., Zsoter, E.,
- 564 Buontempo, C., and Thépaut, J.-N.: ERA5-Land: a state-of-the-art global reanalysis dataset for land applications,
- 565 Copernicus Climate Change Service (C3S) Climate Data Store (CDS), 2021. Available at:
- 566 <u>https://doi.org/10.24381/cds.e2161bac</u>.
- 567 Murguia-Flores, F., Hodson, A. J., and Thornton, S. F.: Soil Methanotrophy Model (MeMo v1.0): a process-based
- 568 model to quantify global uptake of atmospheric methane by soil, Geosci. Model Dev., 11, 2009-2032,
- 569 https://doi.org/10.5194/gmd-11-2009-2018, 2018.
- 570 NASA Earth Observatory: Why Methane Surged in 2020. Available at:
- 571 <a href="https://earthobservatory.nasa.gov/images/150967/why-methane-surged-in-2020.">https://earthobservatory.nasa.gov/images/150967/why-methane-surged-in-2020.</a>
- 572 NASA Earth Observatory: Intense Flooding in Bangladesh, 1 August 2020. Available at:
- 573 <a href="https://earthobservatory.nasa.gov/images/147057/intense-flooding-in-bangladesh">https://earthobservatory.nasa.gov/images/147057/intense-flooding-in-bangladesh</a>.
- 574 Niwa, Y., Tojima, Y., Terao, Y., Saeki, T., Ito, A., Umezawa, T., Yamada, K., Sasakawa, M., Machida, T.,
- 575 Nakaoka, S.-I., Nara, H., Tanimoto, H., Mukai, H., Yoshida, Y., Morimoto, S., Takatsugi, S., Tsuboi, K., Sawa,
- 576 Y., Matsueda, H., Ishijima, K., Fujita, R., Goto, D., Lan, X., Schuldt, K., Heliasz, M., Biermann, T., Chmura, Ł.,
- 577 Necki, J., Xueref-Remy, I., and Sferlazzo, D.: Multi-observational estimation of regional and sectoral emission
- 578 contributions to the persistent high growth rate of atmospheric CH<sub>4</sub> for 2020–2022, Atmos. Chem. Phys., 25, 6757–
- 579 6785, <a href="https://doi.org/10.5194/acp-25-6757-2025">https://doi.org/10.5194/acp-25-6757-2025</a>, 2025.
- Patra, P. K., Canadell, J. G., Houghton, R. A., Piao, S., Oh, N.-H., Wang, T., Ciais, P., Manjunath, K. R.,
- 581 Bhattacharya, T., Bousquet, P., Chhabra, A., Liu, Y., and Su, Y.: The carbon budget of South Asia,
- 582 Biogeosciences, 10, 513–527, https://doi.org/10.5194/bg-10-513-2013, 2013.
- Peng, S., Lin, X., Thompson, R. L., Xi, Y., Liu, G., Hauglustaine, D., Lan, X., Poulter, B., Ramonet, M., Saunois,
- 584 M., Yin, Y., Zhang, Z., Zheng, B., and Ciais, P.: Wetland emission and atmospheric sink changes explain methane
- 585 growth in 2020, Nature, 612, 477–482, https://doi.org/10.1038/s41586-022-05447-w, 2022.
- 586 Peters, C. N., Bennartz, R., and Hornberger, G. M.: Satellite-derived methane emissions from inundation in
- 587 Bangladesh, J. Geophys. Res.-Biogeosci., 122, 1137–1155, <a href="https://doi.org/10.1002/2016JG003740">https://doi.org/10.1002/2016JG003740</a>, 2017
- 588 Pisso, I., Sollum, E., Grythe, H., Kristiansen, N. I., Cassiani, M., Eckhardt, S., Arnold, D., Morton, D., Thompson,
- 589 R. L., Groot Zwaaftink, C. D., Evangeliou, N., Sodemann, H., Haimberger, L., Henne, S., Brunner, D., Burkhart,
- 590 J. F., Fouilloux, A., Brioude, J., Philipp, A., Seibert, P., and Stohl, A.: The Lagrangian particle dispersion model
- 591 FLEXPART version 10.4, Geosci. Model Dev., 12, 4955–4997, https://doi.org/10.5194/gmd-12-4955-2019,
- 592 2019.
- 593 Raju, A., Halder, S., Tiwari, Y. K., Singh, N., Stroppiana, D., and Jain, M.: Regional estimation of methane
- 594 emissions over peninsular India using atmospheric inverse modelling, Environ. Monit. Assess., 194, 572,
- 595 https://doi.org/10.1007/s10661-022-10323-1, 2022.





- 596 Rocher-Ros, G., Sponseller, R. A., and Giesler, R.: Global methane emissions from rivers and streams, Nat.
- 597 Geosci., 16, 123–130, https://doi.org/10.1038/s41586-023-06344-6, 2023.
- 598 Schneising, O., Buchwitz, M., Reuter, M., Bovensmann, H., and Burrows, J. P.: Advances in retrieving XCH4 and
- 599 XCO from Sentinel-5 Precursor: improvements in the scientific TROPOMI/WFMD algorithm, Atmos. Meas.
- 600 Tech., 16, 123–145, https://doi.org/10.5194/amt-16-669-2023, 2023.
- 601 Seibert, P., and Frank, A.: Source-receptor matrix calculation with a Lagrangian particle dispersion model in
- backward mode, Atmos. Chem. Phys., 4, 51–63, https://doi.org/10.5194/acp-4-51-2004, 2004.
- 603 Singh, A., Kuttippurath, J., Abbhishek, K., Mallick, N., Raj, S., Chander, G., and Dixit, S.: Biogenic link to the
- 604 recent increase in atmospheric methane over India, J. Environ. Manage., 289, 112526,
- 605 <u>https://doi.org/10.1016/j.jenvman.2021.112526</u>, 2021.
- 606 Stavert, A. R., Saunois, M., Canadell, J. G., Poulter, B., Jackson, R. B., Régnier, P., Lauerwald, R., Raymond, P.
- 607 A., Allen, G. H., Patra, P. K., Bergamaschi, P., Bousquet, P., Chandra, N., Ciais, P., Gustafson, A., Ishizawa, M.,
- 608 Ito, A., Kleinen, T., Maksyutov, S., McNorton, J., Melton, J. R., Müller, J., Niwa, Y., Peng, S., Riley, W. J.,
- 609 Segers, A., Tian, H., Tsuruta, A., Yin, Y., Zhang, Z., Zheng, B., and Zhuang, Q.: Regional trends and drivers of
- the global methane budget, Global Change Biol., 28, 182–200, https://doi.org/10.1111/gcb.15901, 2022.
- 611 Tarantola, A.: Inverse Problem Theory and Methods for Model Parameter Estimation, Society for Industrial and
- Applied Mathematics, Philadelphia, PA, 358 pp., 2005.
- 613 Thompson, R. L., and Stohl, A.: FLEXINVERT: an atmospheric Bayesian inversion framework for determining
- 614 surface fluxes of trace species using an optimized grid, Geosci. Model Dev., 7, 2223-2242,
- 615 https://doi.org/10.5194/gmd-7-2223-2014, 2014.
- Thompson, R. L., Krishnankutty, N., Pisso, I., Schneider, P., Stebel, K., Sasakawa, M., Stohl, A., and Platt, S.:
- 617 Efficient use of a Lagrangian Particle Dispersion Model for atmospheric inversions using satellite observations of
- 618 column mixing ratios, Atmos. Chem. Phys., 25, 12737–12751, https://doi.org/10.5194/acp-25-12737-2025, 2025.
- 619 Wang, F., Maksyutov, S., Janardanan, R., Tsuruta, A., Ito, A., Morino, I., Yoshida, Y., Tohjima, Y., Kaiser, J. W.,
- 620 Janssens-Maenhout, G., Lan, X., Mammarella, I., Lavric, J. V., and Matsunaga, T.: Interannual variability on
- methane emissions in monsoon Asia derived from GOSAT and surface observations, Environ. Res. Lett., 16,
- 622 024040, <a href="https://doi.org/10.1088/1748-9326/abd352">https://doi.org/10.1088/1748-9326/abd352</a>, 2021.
- 623 Weber, T., Wiseman, N. A., and Kock, A.: Global ocean methane emissions dominated by shallow coastal waters,
- Nat. Commun., 10, 4584, <a href="https://doi.org/10.1038/s41467-019-12541-7">https://doi.org/10.1038/s41467-019-12541-7</a>, 2019.
- 625 Wiedinmyer, C., Akagi, S., Yokelson, R. J., Emmons, L. K., Al-Saadi, J. A., Orlando, J. J., and Soja, A. J.: The
- 626 Fire Inventory from NCAR version 2.5: an updated global fire emissions model for climate and chemistry
- 627 applications, Geosci. Model Dev., 16, 123–145, <a href="https://doi.org/10.5194/gmd-16-3873-2023">https://doi.org/10.5194/gmd-16-3873-2023</a>, 2023.

https://doi.org/10.5194/egusphere-2025-5108 Preprint. Discussion started: 14 November 2025 © Author(s) 2025. CC BY 4.0 License.





628	Worden, J. R., Bowman, K. W., and Bloom, A. A.: The 2019 methane budget and uncertainties at $1^{\circ}$ resolution
629	and each country through Bayesian integration of GOSAT total column methane data and a priori inventory
630	estimates, Atmos. Chem. Phys., 22, 6811–6841, https://doi.org/10.5194/acp-22-6811-2022, 2022.
631	Yu, X., Millet, D. B., Henze, D. K., Turner, A. J., Delgado, A. L., Bloom, A. A., and Sheng, J.: A high-resolution
631 632	Yu, X., Millet, D. B., Henze, D. K., Turner, A. J., Delgado, A. L., Bloom, A. A., and Sheng, J.: A high-resolution satellite-based map of global methane emissions reveals missing wetland, fossil fuel, and monsoon sources,